Heat transport driven by the ITG and ETG instabilities in ASDEX Upgrade H-modes

F. Ryter[1], C. Angioni[1], M. Dunne[1], R. Fischer[1], B. Kurzan[1], A. Lebschy[1], R.M. McDermott[1], W. Suttrop[1], G. Tardini[1], E. Viezzer[2], M. Willensdorfer[1] and the ASDEX Upgrade Team[1]‡

[1] Max-Planck-Institut für Plasmaphysik Garching, Germany

[2] Dept. of Atomic, Molecular and Nuclear Physics,University of Seville Seville, Spain

E-mail: ryter@ipp.mpg.de

Abstract.

A study of the properties of the turbulence-driven ion and electron heat fluxes, is presented. Dedicated H-mode experiments taking advantage of the on-axis and off-axis possibilities of both neutral beam injection and electron cyclotron resonance heating available on the ASDEX Upgrade tokamak were carried out. The experimental results are interpreted by comparisons with gyrokinetic calculations. Ion heat transport is, as expected, driven by the Ion Temperature Gradient (ITG) instability with the features predicted by theory: increase of the driven heat flux above a threshold in normalised gradient. In addition the main effects known to impact on the stability of the turbulence, temperature ratio and fast ions population, are exhibited by the experimental results and agree with the gyrokinetic calculations. It is known that the ITG also contributes to the electron heat flux, but that an electron instability can be required in addition when the ITG contribution does not drive the whole imposed electron heating. This situation, investigated by adding electron cyclotron heating, indicates that in the experiments presented here the Electron Temperature Gradient instability develops.

1. Introduction

It is widely accepted that turbulence-driven ion heat transport in MHD quiescent tokamak H-mode plasmas is mostly driven by the ion temperature gradient (ITG) instability. But the ITG

‡ see A. Kallenbach et al. Nuclear Fusion 57 (2017) 10201

also drives a certain amount of electron heat flux, roughly proportional to the driven ion heat flux with some variations depending on the plasma parameters. In addition, contributions to the electron heat flux from trapped electron mode (TEM) and/or electron temperature gradient (ETG) instabilities are expected if the ITG is not sufficient to drive the electron heat flux imposed by the applied heating power. Kinetic ballooning modes do not contribute in the present study because the beta value is rather low: $\beta_N \leq 1.3$ and $q^2\beta_e \leq 2.1\%$ at the position of the analyses presented below. According to theory, these three instabilities (ITG, TEM and ETG) have the common property to appear above their respective threshold in normalised temperature gradient ($R/L_T = -R\nabla T/T$), R being the major radius, T the ion temperature (T_i) for the ITG and the electron temperature (T_e) for TEM and ETG. When R/L_T is increased, the heat flux driven by each of these instabilities (q_i or q_e) increases above the corresponding threshold (R/L_{T_c}) with a slope which characterises the so-called stiffness. A strong stiffness implies large variations of the heat flux for small variations in R/L_T such that the corresponding temperature profiles remain very close to the threshold. Conversely, in cases of weak stiffness larger excursions in R/L_T above R/L_{T_c} are expected.

In the present work we describe and discuss the experimental investigations carried out in the ASDEX Upgrade (AUG) tokamak to assess the relative role of these different contributions to heat transport and investigate threshold and stiffness in comparisons with gyrokinetic calculations.

For this purpose we performed dedicated H-mode experiments using the experimental possibilities available on the device, namely neutral beam injection (NBI) which heats both electrons and ions, as well as electron cyclotron resonant heating (ECRH) which heats exclusively the electrons. For both heating methods the power can be deposited centrally or off-axis allowing us to vary the heat flux at a given radial position between the two depositions. The sum of the heating power outside of the off-axis deposition is thus kept almost roughly constant there such that the temperatures vary little. This is important because this implies that the boundary condition of the temperature profiles outside of the region where the analysis is performed is kept constant. This is a now well established method to investigate heat transport, threshold and stiffness, as done in particular for the electron channel [1, 2, 3, 4, 5].

In addition, modulating the electron temperature with ECRH provides data for the so-called

transient transport which yields directly the slope of the stiffness curve for electron heat transport, because of the dependence of q_e on ∇T_e [6, 7, 8, 9]. From the modulation data the electron heat pulse diffusivity (χ_e^{HP}) is deduced, complementary to the power balance diffusivity (χ_e^{PB}), related by $\chi_e^{HP} = \chi_e^{PB} + (\partial\chi_e/\partial(\nabla T_e))\nabla T_e$. If TEM and/or ETG modes contribute to the electron heat transport above their threshold a variation of the electron heat flux and concomitantly of R/L_{T_e} should reveal a strong increase of χ_e^{HP} at their threshold due to the sudden change of $\partial\chi_e/\partial(\nabla T_e)T_e$ and χ_e^{HP} remains much larger than χ_e^{PB} if R/L_{T_e} is further increased. This has been clearly demonstrated in AUG for TEM-dominated plasmas [10, 1, 11]. If the ITG instability only is the main drive of the electron heat flux, χ_e^{HP} remains low and very close to χ_e^{PB}, because q_e driven by the ITG depends very weakly on ∇T_e, as shown for AUG in [11].

Similarly, a modulation of the ion temperature is in principle also possible, as shown in [12], but does not yield sufficiently accurate data when done with NBI in AUG and was not attempted in these experiments.

The experiments described in the present paper are based on these properties. The experimental data are provided by the usual diagnostics, in particular the 60 channel Electron Cyclotron Emission (ECE) radiometer complemented by the Thomson scattering for T_e, Interferometry, Thomson scattering and Lithium beam for density. Electron temperature and density measurements are analysed in a combined way with the Integrated Data Analysis (IDA) which yields consistent profiles of T_e and n_e [13, 14, 15]. The measurements of T_i and rotation are provided by the Charge Exchange Recombination Spectroscopy (CXRS) using two of the NBI beams, [16, 17, 18]. The heating power deposition calculations and power balance analyses are performed with the TRANSP code [19, 20]. Two distinct series of H-mode experiments with similar parameters were carried out to investigate the ion and electron channels respectively, as described in the next two sections. The paper is completed by a discussion.

2. Ion heat channel

The stability of the ITG depends on several plasma quantities: T_e/T_i, R/L_{T_e}, R/L_n, β, radial shear of the toroidal rotation, ion dilution by impurities or fast ions, stabilisation by fast ions.

These dependences affect the stiffness and/or the threshold of the instability as follows:
- T_e/T_i is destabilising such that the stiffness increases and the threshold decreases when T_e/T_i increases, [21, 22, 23, 24] as well as [25] and references therein. R/L_{T_e} and R/L_n are also destabilising for the ITG when the effects of kinetic electrons are taken into account.
- The threshold also increases with normalised shear $\hat{s}/q$, [26].
- High shear of the toroidal rotation is stabilising and increases the threshold [27];
- Fast ion effects reduce the stiffness and increase the threshold trough ion dilution [28] linear and non-linear effects, in particular at high β, [29, 30, 31, 32, 33].

2.1. Experimental results

In our experiments to the ITG-driven ion heat flux, we made use of the possibilities offered by the NBI system. It consists of eight beams injecting each 2.5 MW with different geometries such that two of them deposit their power with a maximum at about mid-radius and are labelled here "off-axis", while the deposition of the other six beams occurs centrally and these are named "on-axis". We performed H-mode plasmas in the usual range of ASDEX Upgrade with $P_{NBI} \approx 5MW$, plasma current of 0.8 MA at a magnetic field of 2.6 T, yielding $q_{95} \approx 5$, at a line averaged density of about 6 $10^{19}\mathrm{m}^{-3}$, corresponding to a Greenwald fraction of about 0.55. These deuterium plasmas were quite pure with $Z_{eff} \approx 1.1$. The aim was to vary the ion heat flux in the central region by applying either on-axis or off-axis NBI. We used two NBI beams combined in the following three ways: the extremes cases, two off-axis or two on-axis, or an intermediate configuration with one off-axis and one on-axis beam which we labelled "mixed" in the remaining of the paper. During the off-axis phase short NBI blips were made with on-axis beams for the CXRS diagnostics. In addition ECRH power was also deposited in the plasma centre, at two different levels: 0.65 MW or 2.75 MW kept constant throughout the discharges. The lowest power was used to avoid tungsten accumulation during the NBI off-axis phases, the higher level to also increase T_e/T_i and study its impact on the ITG. The phases with on-axis and mixed NBI were sawtoothing but not the off-axis ones.

The case with $P_{ECRH} = 0.65$ MW is illustrated in figure 1 for the three NBI combinations for different profiles. The radius used for the horizontal axis is the usual normalised toroidal flux , ρ_{tor}. The power density in the ion channel plotted in panel (a) shows that, as expected

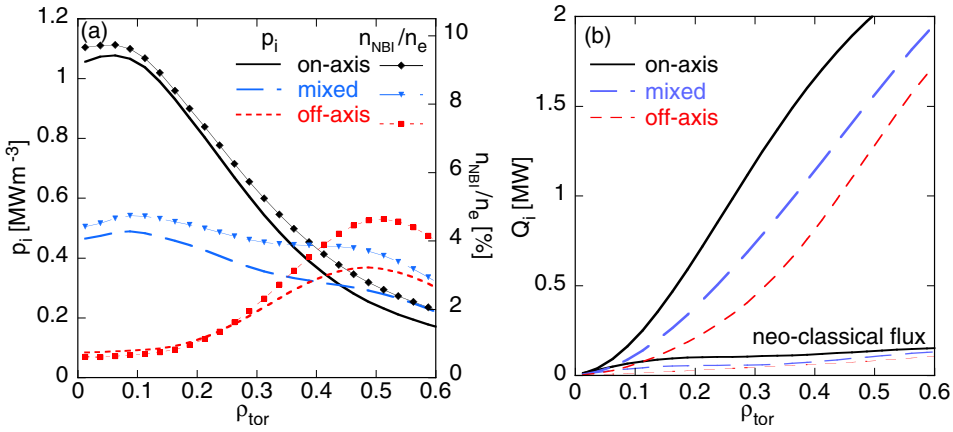

Figure 1. Ion power deposition and heat profiles in the central region ($\rho_{tor} \leq 0.6$) for the on-axis, off-axis and mixed NBI cases, for the case $P_{ECRH} = 0.65$ MW. Panel (a): Ion heat and NBI fast ion density normalised by the electron density. Panel (b): Total surface-integrated ion heat flux. The contribution from neo-classical transport is indicated.

for the off-axis case, the ion heat power deposition is low in the central region, $\rho_{tor} \leq 0.4$. It clearly increases for the mixed and on-axis cases. The analysis must therefore be carried out in this region to have a large variation in ion heat flux including a low value in the purely off-axis case to approach the ITG threshold in R/L_{T_i}. The corresponding variation of the surface-integrated ion heat flux (Q_i) is shown in plot (b), indicating that a variation of Q_i of about a factor of three could be achieved in the inner region, at $\rho_{tor} \approx 0.3$. We also plot the heat flux driven by neo-classical transport which is much smaller than that the total flux, showing that turbulent transport dominates. In the following we label turbulent transport the quantity $Q_{i,turb} = Q_i - Q_{NC}$ for comparisons with the gyrokinetic calculations.

For completeness, we also show in figure 2 the electron power deposition and heat fluxes for the low ECRH power case corresponding to the ion values displayed in figure 1. Plot (a) shows clearly the peaked ECRH deposition while the lower values reflect the variations of the sum of the other contributions (Ohmic, NBI and energy exchange) for the 3 NBI configurations. The surface-integrated heat fluxes of plot (b) indicate that Q_e is higher than Q_i (figure 1 b) in the region of interest, around $\rho_{tor} = 0.3$. This explains the fact that in our experiments T_e/T_i is always above 1 as will be seen in the following.

Figure 3 shows the corresponding variations of the T_e and T_i profiles for the three NBI cases and for each of the two ECRH powers. Here also we focus on the central region of the

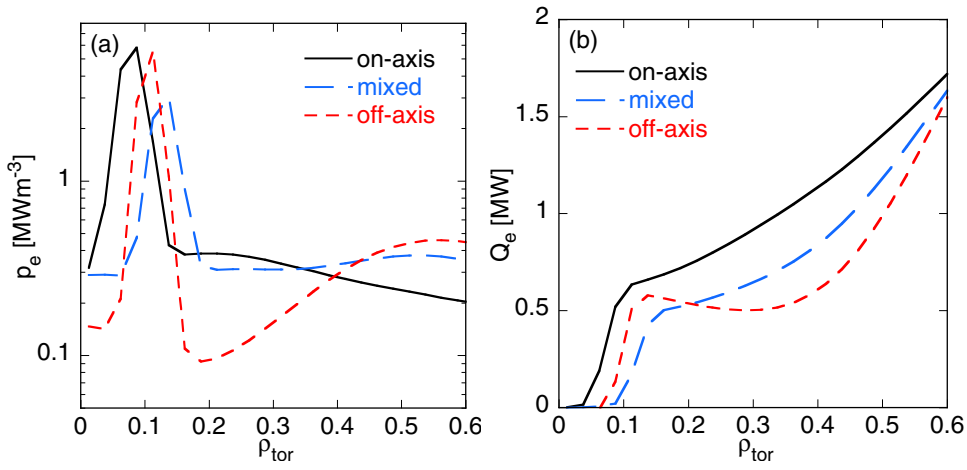

Figure 2. Electron power deposition and heat profiles in the central region ($\rho_{tor} \leq 0.6$) for the on-axis, off-axis and mixed NBI cases, for the case $P_{ECRH} = 0.65$ MW. Panel (a): Electron power deposition profile. Panel (b): Total surface-integrated electron heat flux.

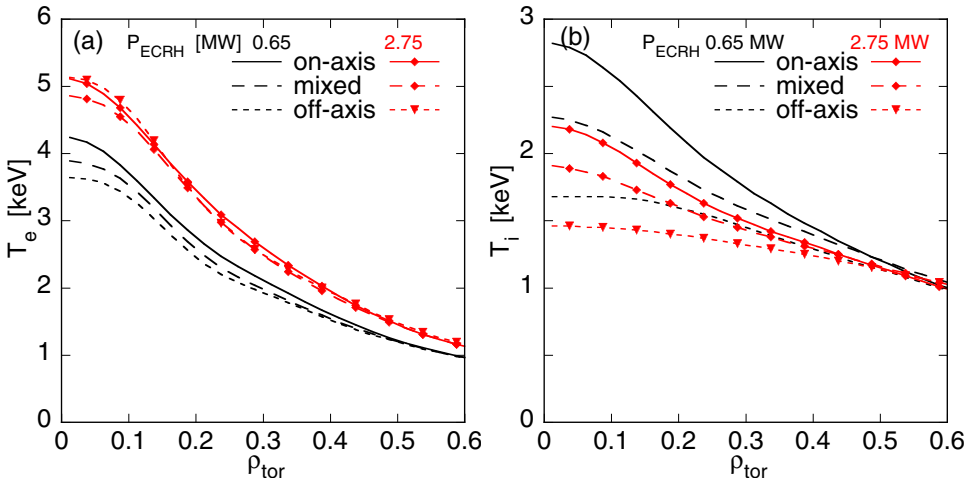

Figure 3. T_e and T_i profiles for on-axis, off-axis and mixed NBI deposition for the two P_{ECRH} powers, plotted in the central region, $\rho_{tor} \leq 0.6$. These are the fits used for the TRANSP calculations. For clarity the experimental data points are not shown. The dots on some of the profiles are not measured data but only for easier identification of the profiles.

plasma where the flux variations are the largest and show the profiles for $\rho_{tor} \leq 0.60$. The T_e profiles displayed in panel (a) are clearly higher for P_{ECRH} = 2.75 MW compared to 0.65 MW and in both cases the variations due the different NBI cases are small. In contrast, as expected, the T_i profiles react clearly to the NBI configuration in the radial region of interest, $0.20 \leq \rho_{tor} \leq 0.40$. The values of T_i are higher for the on-axis case, but more important

is the fact that for the off-axis cases (low Q_i) the profiles are much flatter: low T_i gradient. Overall, the T_i profiles for the high P_{ECRH} cases are lower than for the low power case. We will show later that this is consistent with the high T_e/T_i which destabilises the ITG. Further, it is worth underlying that, corresponding to the design of these experiments, T_i at $\rho_{tor} \geq 0.5$ is almost constant independently of the heat scheme which is expected because the ion heat flux varies little in the outer part of the plasma in the shift of the power from on-axis to off-axis. As already pointed out above, this is important because the value of T_i at mid radius is the boundary condition for the T_i profiles further in. Therefore, in the region of analysis the T_i profiles are solely determined by transport and heat flux and not by an external condition, e.g. pedestal top. This indicates that the experiments worked as expected. Not shown here are the profiles of the toroidal plasma rotation which are very flat in the off-axis case but rather peaked in the on-axis case.

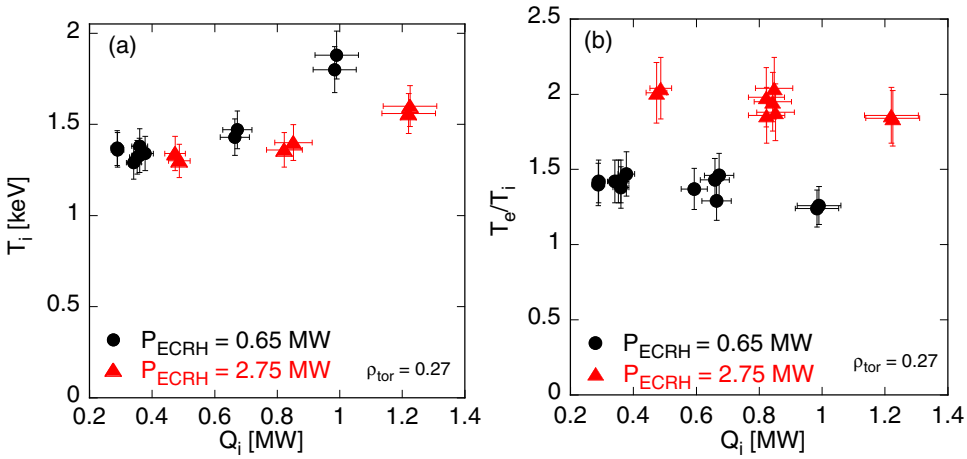

Figure 4. Panel(a): variation of T_i at $\rho_{tor} = 0.27$ versus ion heat flux for the three NBI variations for each of the two cases with low and high ECRH power, 0.65 and 2.75 MW respectively. Panel (b), corresponding values of T_e/T_i.

We made the analysis of the dependence of the ion heat flux upon R/L_{T_i} at $\rho_{tor} \approx 0.27$ which is the radial position at the which the gyrokinetic calculations presented below have also been performed. The results for the two cases with P_{ECRH} 0.65 MW and 2.75 MW are shown in the next figures. Figure 4 (a) illustrates the behaviour of T_i at $\rho_{tor} = 0.27$ for the three NBI cases and the two ECRH cases respectively. As already indicated above, the overall variation is moderate, whereby the largest change corresponds to the on-axis NBI cases with the highest

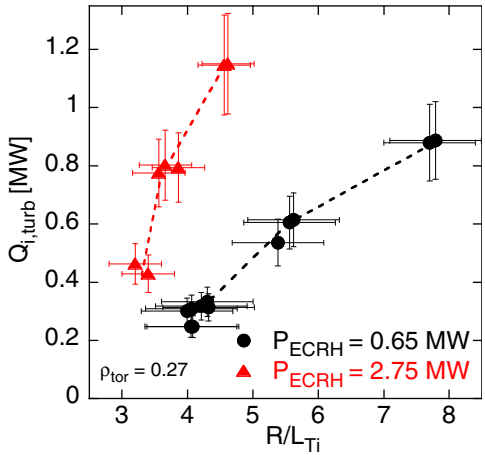

Figure 5. Experimental surface-integrated ion heat flux at $\rho_{tor} = 0.27$ provided by the power balance analysis plotted versus R/L_{T_i} for the three different NBI depositions and the two ECRH powers. The lines are only to guide the eye and have no physics meaning.

Q_i value, for which T_i is clearly higher than the other two cases of the corresponding ECRH power. We will come back to this when discussing the gyrokinetic calculations. Figure 4 (b) indicates that, as expected, T_e/T_i is clearly larger for the P_{ECRH} = 2.75 MW case, but the variation of T_e/T_i with Q_i is moderate for each of the two ECRH cases. This is important for the analysis as the impact of T_e/T_i on the ITG stability remains weak for each of the P_{ECRH} cases but might be large between the two ECRH cases.

The relation between ion flux and R/L_{T_i} is shown in figure 5 for the surface-integrated turbulent flux. It reveals in both ECRH cases a clear increase of the heat flux with R/L_{T_i} induced by the three NBI combinations, from low to high heat flux corresponding to off-axis, mixed and on-axis respectively. This behaviour is in agreement with the expectation that the ITG is destabilised above a threshold and that the ITG-driven flux increases with R/L_{T_i} above this threshold. The plot also suggests a trend for $Q_{i,turb}$ to saturate towards higher R/L_{T_i} which will be discussed later. For the highest value of P_{ECRH} the heat flux is higher which is due to the additional contribution of P_{ECRH} through the energy exchange which flows from the electron to the ion heat channel, T_e being significantly higher than T_i in all the cases. There is also a small increase from the NBI ion heating due to the higher T_e. Important is to note the steeper increase of the ion heat flux with R/L_{T_i} for the case with higher P_{ECRH}, revealing a clearly higher stiffness, attributed to the destabilisation of the ITG instability induced by the

higher T_e/T_i, as will be confirmed below. The effect of the stiffness on the ion temperature profiles is obviously strong: at high T_e/T_i the variation in R/L_{T_i} just reaches 1.3 and its maximum value is 4.3, while in contrast at lower T_e/T_i the variation in R/L_{T_i} is about 3.5 and a maximum of 7.8 is reached.

To compare the properties of turbulent transport under different conditions the heat flux is usually normalised to the gyro-Bohm transport. The normalisation is $q_{i,gB} = 2\sqrt{2}T_i^{2.5}n_i m_i^{0.5}/(e^2B^2R^2)$, with n_i and m_i being ion density and mass respectively, e the elementary charge and B magnetic field. The normalisation is made on the ion heat flux in Wm^{-2}. The numerical factor $(2\sqrt{2})$ reflects the fact that the calculation of the ion thermal velocity includes a $\sqrt{2}$ factor. The gyro-Bohm normalisation has the advantage of cancelling the impact of the variations in T_i which is strong due to the $T_i^{2.5}$ dependence, if transport is indeed purely of gyro-Bohm type. In the present case $T_i^{2.5}$ is by far the strongest impact of the normalisation. The normalised ion heat flux for our experiments is shown in figure 6. The points corresponding to the low ECRH power case exhibit a clear saturation towards the highest values of R/L_{T_i}. The value of $q_{i,gB}$ for the on-axis case is even lower than that of the mixed case. This is the impact of $T_i^{2.5}$ through the high value of T_i revealed by figure 4 (a). This saturation suggests a strong reduction of the stiffness for the on-axis NBI case, which is reflected by the higher values of both T_i and R/L_{T_i}, as will be confirmed by the gyrokinetic simulations presented in the next sub-section. The cases with high ECRH power exhibit only a rather weak saturation, due to the fact that T_i varies little for the three NBI configurations. Apart from the saturation, the gyro-Bohm normalisation does not change the general features compared to the plot of the surface integrated flux. In particular the differences between the two sets with low and high ECRH power are confirmed.

2.2. Results from gyrokinetic calculations

To interpret the above results we performed non-linear gyrokinetic calculations with the GKW code [34]. The calculations include, collisions, electro-magnetic effects, effect of toroidal rotation and NBI fast ions. The ITG stabilisation by the fast ions discussed below includes both dilution and electro-magnetic effects. The non-linear calculations are demanding in computing time and power, in particular when fast ions are included, such that the number

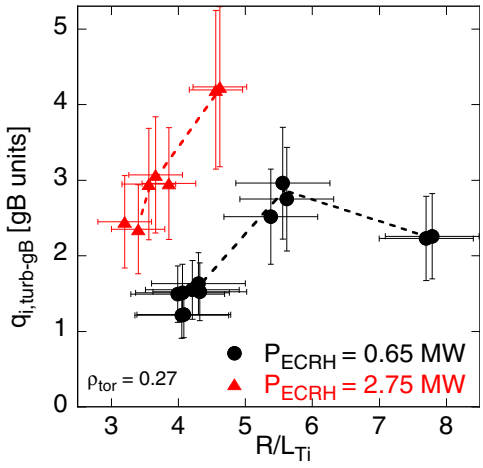

Figure 6. Experimental ion heat flux in gyro-Bohm units versus R/L_{T_i} at $\rho_{tor} = 0.27$ for the three different NBI depositions and the two ECRH powers. The lines are only to guide the eye and have no physics meaning.

of such calculations must be restricted to the most important cases. The calculations for the ion heat flux treated in this section were performed in the range of the long turbulence wavelengths corresponding to that of the ITG. They were carried out with a resolution of 43 toroidal modes and 339 radial modes in a box with size of 80 ρ_i and 105 ρ_i in the radial and binormal directions respectively, allowing to solve up to $k_y\rho_i = 2.5$ with the smallest non-zero $k_y\rho_i = 0.06$, as well as up to $k_x\rho_i = 13.6$ with a minimum non-zero $k_x\rho_i = 0.080$, with $\rho_i = \sqrt{2m_iT_i}/eB$. Moreover, 32 grid points have been used along the field line and the velocity space is discretised with 20 points for the magnetic moment and 48 points and 2 signs for the parallel velocity. They include two species or three when the NBI fast ions are taken into account. The runs were done for the two ECRH powers of 0.65 MW and 2.75 MW, $\rho_{tor} = 0.27$ corresponding to the same cases and at the same radial position as presented above for the experimental analysis. The experimental data required as input were taken as a representative average of the corresponding experimental values. The main quantities which vary in the experiments are the temperature gradients, the heat fluxes and the NBI ion population. It should be pointed out that the electron and ion densities, as well as their normalised gradients, vary little, without any recognisable trend depending on the NBI configuration or ECRH power. This is attributed to the rather high density at which these experiments have been carried out. In particular R/L_{n_e} is close to 2.1 ± 0.15 in all the experimental cases. We

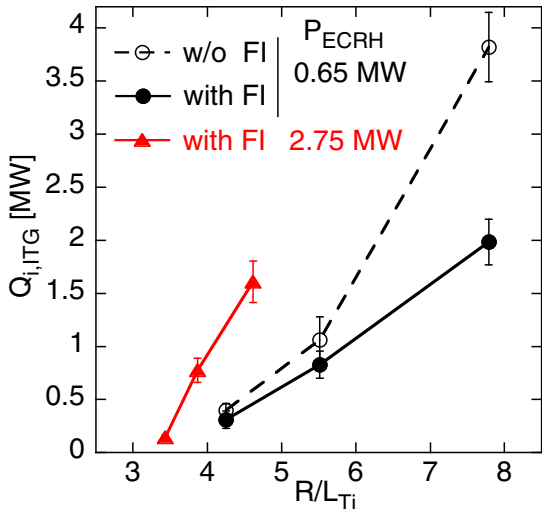

Figure 7. Surface-integrated ion heat flux yielded by the gyrokinetic calculations versus R/L_{T_i} at $\rho_{tor} = 0.27$ for the three different NBI depositions and the two ECRH powers. For $P_{ECRH} = 0.65MW$ the results with and without fast ions (FI) are shown. The lines are only to guide the eye and have no physics meaning.

have also verified with linear gyrokinetic calculations that this value is not high enough to destabilised the ubiquitous mode. Therefore one does not expect any change of turbulence type due to variations of the density profile between the different heating cases.

The results from the non-linear calculations are shown in figure 7 which displays the calculated surface-integrated ion heat flux versus R/L_{T_i}. The error bars represent the standard deviation of the calculated flux during a sufficiently long time interval at saturation. We first focus on the cases with low ECRH power for which we show calculations including the effect of the NBI fast ions (solid circles and lines) or not (open circles and dashed lines). These indicate that taking the NBI fast ions into account reduces the ion heat flux due to the stabilisation of the ITG. Whereas this effect is almost negligible for the off-axis and weak for the mixed NBI case, it is strong for the on-axis case: the ion heat flux is reduced by about a factor of two when the NBI fast ions are taken into account. This is consistent with the larger population of fast ions at $\rho_{tor} = 0.27$, shown in figure 1 (a) and in line with previous results [29, 30, 31, 32, 33].

It should be mentioned that, despite the rather high value of the toroidal rotation shear for the on-axis case, the calculated impact of the $E \times B$ stabilisation remains weak. We attribute

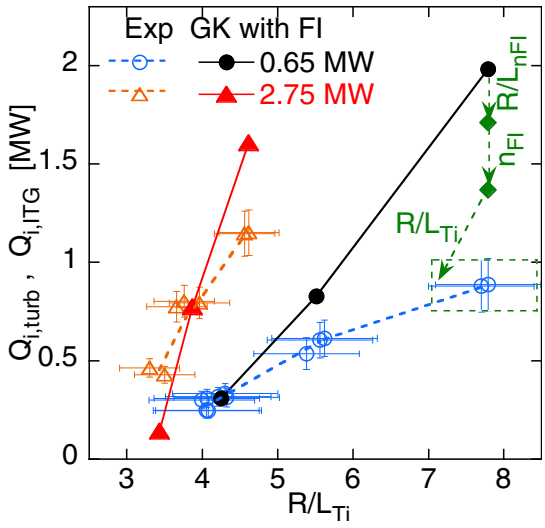

Figure 8. Comparison of gyrokinetic calculations including the NBI fast ions and experimental results at $\rho_{tor} = 0.27$ for the cases presented in the previous figures. The diamonds and arrows represent the gyrokinetic sensitivity scan described in the text: the vertical arrow (FI) displays the 16% reduction of Q_i corresponding to a 20% increase of the gradient of the NBI fast ion density, the oblique one the reduction corresponding to a decrease of R/L_{T_i} within the experimental error bars.

this to the fact that the value of $\varepsilon/q = 0.066$ (ε being the aspect ratio and q the safety factor), which directly determines the strength of this effect, is indeed small in the central region of the plasma where we make the analysis, due to the low value of ε.

The results for the case with higher ECRH power are also displayed in figure 7, but, to limit the number of calculations, only represented by the modelling including the NBI ions. Similarly to the experimental results, the increase of the ion heat flux with R/L_{T_i} is much stronger than for the case with low P_{ECRH}, indicating a higher stiffness caused by the higher value of T_e/T_i.

The direct comparison of these calculations including the fast ions with the experimental results is shown in figure 8. Focusing first on the cases with low ECRH power: the agreement between simulations and experiments is rather good for the off-axis and mixed cases, but for the on-axis case the calculations yield a value of Q_i which is about a factor of two above the experimental value. It should be underlined that, for the NBI on-axis case with a centrally peaked profile of the fast ion density (see figure 1) there are uncertainties on both the fast ion density and its gradient at the position of our analysis which is on the flank of the profile.

Therefore a sensitivity study has been carried out with non-linear gyrokinetic calculations of the on-axis case by varying separately the density of the NBI fast ion population (n_{FI}) and its gradient ($R/L_{n_{FI}}$). The increase of $R/L_{n_{FI}}$ by 25% reduces Q_i by about 16% and an additional increase of n_{FI} by 25% further reduces Q_i by 20%. This reduction of about 30% brings the calculated value of Q_i much closer to the experimental value as illustrated in figure 8 by the two vertical arrows and the corresponding diamonds. The uncertainties on n_{FI} and $R/L_{n_{FI}}$ may arise from various experimental uncertainties but also from the effect of the sawteeth which redistribute the fast ions from inside to outside of the $q = 1$ surface which is located at $\rho_{tor} \approx 0.2$. Another source of uncertainties in the comparison between experiment and modelling is R/L_{T_i}. Indeed, a scan in R/L_{T_i} indicates that the calculated Q_i value is very sensitive to it: a reduction of R/L_{T_i} within the experimental error bars (-0.7) leads a strong reduction of Q_i as underlined by the oblique arrow drawn in figure 8. Adding these three effects of the uncertainties, which is the most optimistic assumption, leads to a Q_i value which agrees with the experimental value within the error bars indicated by the rectangle around the experimental point. For completeness, an extension of this sensitivity study with linear gyrokinetic calculations whose ion heat flux was calibrated on the non-linear calculations indicates that the temperature of the fast ion population (T_{FI}) has no effect on the fast ions stabilisation. The variation of T_{FI} (7 - 15 keV) was performed around the nominal T_{FI} value of 11 keV and did not address possible effects of T_{FI} being close to the thermal temperature or representative of alpha particles of a fusion reactor.

We now consider the cases with high T_e/T_i plotted in figure 8: the agreement of the calculation with the experiment is overall better than for the low T_e/T_i. It is, in particular, important to underline that the higher stiffness caused by the higher T_e/T_i is well reproduced. This can be due to the direct actual impact on the ITG turbulence properties but in addition one might speculate that the fast ion stabilisation itself is reduced at higher Te/Ti. Dedicated linear gyrokinetic calculations with and without fast ions performed to address this question did not exhibit any trend in this direction. Attempted non-linear simulations did not reach a convincingly long steady saturated state and this hypothesis is not excluded. Furthermore, it seems that this investigation and the assessment of the results should probably also include both the role of nonlinearly excited energetic particle driven modes [35] and an

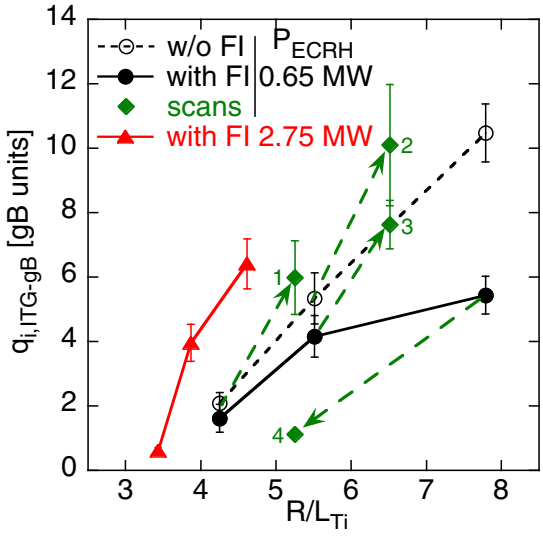

Figure 9. Ion heat flux in gyro-Bohm units from the gyrokinetic calculations corresponding to the cases of figure 7. The four diamonds (labelled 1-4) correspond to the fictive change of R/L_{T_i} indicated by the arrows and described in the text.

increased influence of trapped electron dynamics in ITG turbulence. Such an extensive gyrokinetic study is out of the scope of the present paper and should be presented in another dedicated work. Figure 8 shows also that for the mixed and on-axis cases the calculated and experimental values of Q_i agree well. It should be pointed out here that as the stiffness is high, the heat flux reacts strongly to small variation in R/L_{T_i} such that variations of R/L_{T_i} within the experimental uncertainties have a large impact on the calculated heat flux. This strongly reduces the accuracy of the comparison between the calculated and experimental stiffness values, which is a general issue, see e.g. [32, 31].

As next step of the analysis we now consider the ion heat flux from the gyrokinetic calculations normalised to the gyro-Bohm transport, shown in figure 9. The saturation towards higher R/L_{T_i} values (on-axis NBI) is clear but weaker that for the experimental points which is due to the fact that, in particular for the low P_{ECRH} case, the calculated heat flux is too high, as shown by the previous figure. To better assess the stiffness, we made one fictive scan in R/L_{T_i} for each of the three NBI configurations at low ECRH power: all the parameters of each point were kept constant, except R/L_{T_i} which was increased for the off-axis and mixed cases and reduced for the on-axis case. This is illustrated by the four arrows towards the each of the fictive points represented by diamonds in figure 9 and labelled from 1 to 4. We

first focus on arrows 1 and 2 corresponding to the off-axis and mixed cases without fast ions. They have almost the same slope indicating therefore the same stiffness for these two points, in agreement with the fact that the plasma parameters impacting on the stability of the ITG are very similar, except R/L_{T_i} which is increased on purpose. The fact that their slopes are steeper than the dashed line which connects the open circles representing the calculated points is caused by the slightly different T_i values (see figure 4). We consider now arrows 1, 3 and 4 which correspond to cases calculated including the fast ions whereas for the off-axis case the fast ion effect is negligible such that arrow 1 can be considered. For the mixed case, arrow 3 has a somewhat flatter slope that arrows 1 and 2 due to the rather small but measurable impact of the fast ions. The slope of arrow 4 is much flatter than 1 and 3 which is mainly due to the strong stabilisation by the fast ions and reflects the weaker stiffness. A small contribution to this flattening is due the somewhat lower value of T_e/T_i. Arrow 4 also suggests a clearly higher value of the threshold $R/L_{T_{i,c}}$ as compared to the other cases, which is indeed expected as a consequence of the stabilisation. Thus, for a given applied ion heat flux, the stabilisation by the fast ions increases T_i through two effects: an increase of R/L_{T_i} by increasing $R/L_{T_{i,c}}$ and an increase of both R/L_{T_i} and T_i by reducing the stiffness. This explains the clearly higher value of T_i measured for the on-axis case shown in figure 4, as already pointed out above.

Furthermore, the four fictive scans demonstrate very clearly that each point corresponds to a different curve in the (q_i, R/L_{T_i}) space which is here mainly due to the stabilisation by the NBI fast ions. This study underlines that the interpretation of experimental results requires comparison with modelling including all the relevant effects. In other words and as already specified for the corresponding plots, the lines connecting the points are only drawn to guide the eye and underline the experimental series but have no physics meaning. In this respect, particularly striking is the line connecting the mixed and on-axis cases. In general, they should not be considered as reflecting quantitatively stiffness and threshold because the points correspond to local plasma parameters affecting the ITG stability which are different and not only due to a change in R/L_{T_i}.

Turning now to the higher ECRH power and higher T_e/T_i cases in figure 9: The three points exhibit a higher stiffness in gyro-Bohm units as compared to the cases with lower T_e/T_i. This is clearly shown by the two line segments connecting the three points at high T_e/T_i

whereby the actual stiffness is expected to be higher because the heat flux of the mixed and on-axis points plotted here is reduced by the fast ion stabilisation with a different magnitude. Therefore, the strong effect of T_e/T_i on stiffness is confirmed by the gyro-Bohm normalisation. It seems to play a stronger role on the T_i profiles than the dependence of $R/L_{T_{i,c}}$ upon T_e/T_i.

3. Electron heat channel

As mentioned in the introduction, the electron heat flux can be driven by the ITG, but the electron instabilities such as TEM and/or ETG can also contribute, in particular if the externally applied electron heat flux cannot be completely driven by the ITG. We will see in this section that applying ECRH power leads to this situation in some cases. To investigate such a situation with gyrokinetic calculations a wide wavelength range from the long ones of the ITG/TEM to the short ones of the ETG is required. Such a multi-scale non-linear calculation is a highly demanding in computer power and time and therefore out of the scope of this work. We restricted the analysis to the linear calculations which are presented below. This section contains two subsections. In the first one we investigate the electron heat transport in the NBI on-axis/off-axis experiments described above and in the second one we described and interpret a dedicated experiment based on a scan of the imposed electron heat flux using ECRH.

3.1. Electron transport in the on-axis/off-axis NBI experiments

We discuss here the electron heat flux in the experiments presented in the previous section. This means that in this study the stability of the ITG varies with the changes of the NBI combination while the electron heat flux, partly (or strongly) imposed by the ECRH power varies little for each of the cases at 0.65 MW or 2.75 MW. As for the ion heat flux, the experimental electron heat flux is yielded by power analysis from TRANSP. Note that the neo-classical electron heat flux is negligible.

The surfaced-integrated electron heat flux taken at $\rho_{tor} = 0.27$ is plotted in figure 10 (a) versus R/L_{T_i} and in panel (b) versus R/L_{T_e} for the two ECRH powers 0.65 MW and 2.75 MW. As could be expected, Q_e is overall much higher for P_{ECRH} = 2.75 MW than for 0.65 MW. For P_{ECRH} = 0.65 MW we observe, above the minimum value determined by the ECRH

power, a moderate increase of Q_e with R/L_{T_i} induced by the variation of the NBI deposition which also heats the electrons. If $P_{ECRH} = 2.75MW$ the electron heat flux is high, dominated by the ECRH and almost independent of the NBI variations whose contribution is small in comparison. As shown by figure 10 (b), for each of the two ECRH powers, the variation in R/L_{T_e} is rather narrow. As a logical consequence of the higher applied electron heating the variation in R/L_{T_e} for P_{ECRH} = 2.75 MW occurs at higher values whereas the variations due to the NBI remain small and within the experimental uncertainties of R/L_{T_e}.

The results yielded by the ITG non-linear gyrokinetic calculations described in the previous section are shown in figure 11 for the electron channel. We remind here that these calculations represent only the electron flux related to instabilities at the ion Larmor radius scales (ITG and TEM) without contribution from instabilities at the electron Larmor radius scales. Panel (a) shows the Q_e values equivalent to the ion heat flux points shown in figure 7. The behaviour is rather similar to that of the ion flux which is explained by the fact that the ITG-driven electron heat flux roughly follows the driven ion flux. Note that the NBI fast ion stabilisation also reduces Q_e. However, it should be pointed out that for the higher ECRH power Q_e is significantly higher than for the low ECRH power, thus reflecting the higher imposed electron heat flux. Therefore the ITG reacts to the electron heating in particular through the higher T_e/T_i and R/L_{T_e}, but we will see below that this is not sufficient in all the

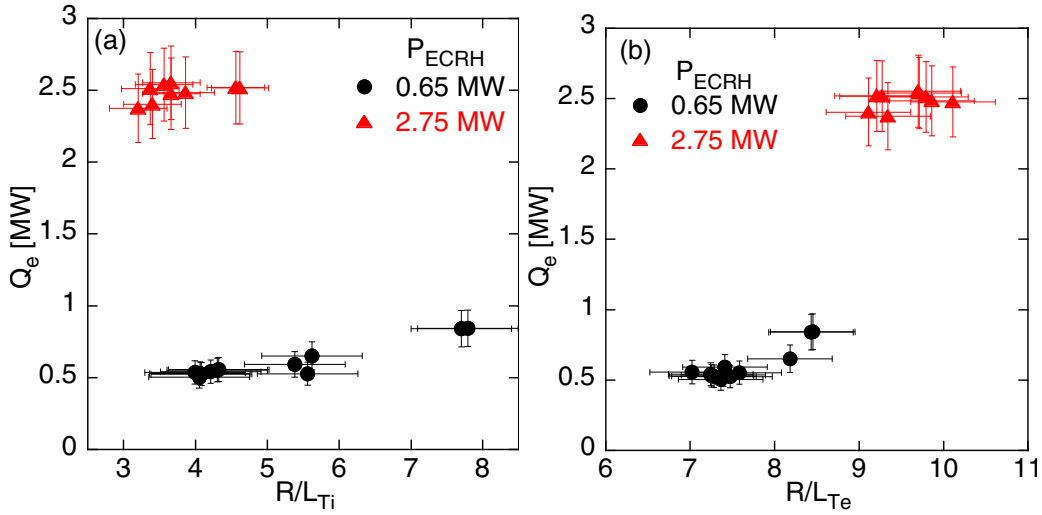

Figure 10. Surfaced-integrated electron heat flux versus R/L_{T_i} for the NBI variations and the two ECRH powers at $\rho_{tor} = 0.27$.

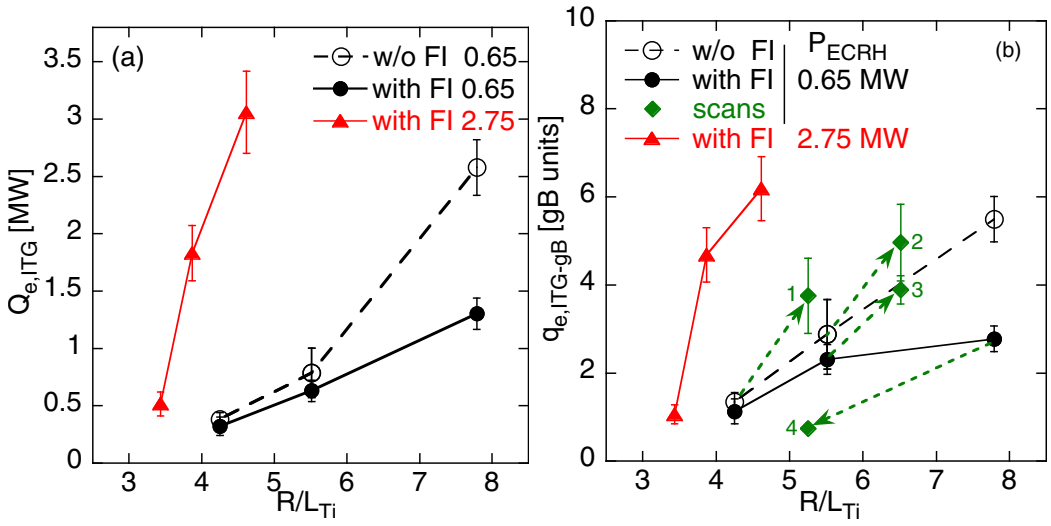

Figure 11. Electron heat flux from gyrokinetic calculations at $\rho_{tor} = 0.27$. Panel (a): surface-integrated flux. Panel(b): flux normalised to gyro-Bohm transport. The scans (1-4) of R/L_{T_i} are also indicated.

cases.

For completeness, we display in panel (b) of figure 11 the heat flux normalised to gyro-Bohm plotted versus R/L_{T_i}. Note here that the gyro-Bohm normalisation is made using $T_e T_i^{1.5}$ instead of $T_i^{2.5}$. As for Q_e, the results are very similar to those of the ion heat flux shown in figure 9, they do not yield noticeable additional information. The saturation for the on-axis NBI case is also present and that the fictive scans in R/L_{T_i} (1 - 4) exhibit a similar picture as that found for the ion heat flux.

More instructive and important is the comparison between the experimental Q_e data and these gyrokinetic results as shown in figure 12. For the NBI on-axis cases of each of the two ECRH powers, which correspond to the highest R/L_{T_i} values, the calculated electron heat flux is comparable to the experimental one within differences which are similar to those found for the ion heat flux. Here also this means that, in the cases with high T_e/T_i values, the high ITG turbulence seems to be sufficient to drive the whole electron heat flux, even in the presence of high ECRH power. In contrast, for the off-axis cases, lowest values of R/L_{T_i} in figure 12, the calculated values of Q_e are clearly lower than the experimental ones, the difference being particularly large for the case with high ECRH power. This is due to the fact that the high electron heat flux imposed by the ECRH power cannot be driven by the instabilities at the ion

wavelength scale only: as R/L_{T_i} is low the ITG is not strongly unstable.

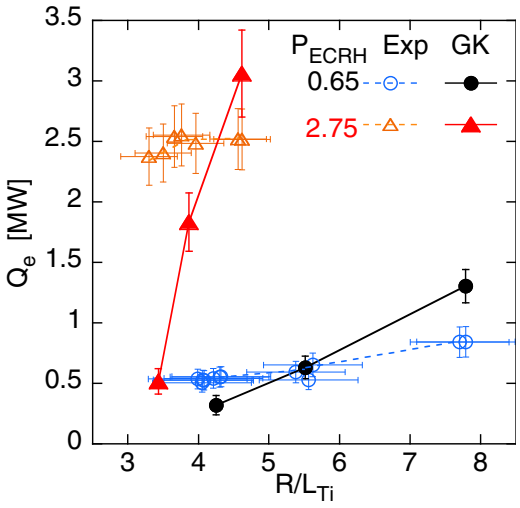

Figure 12. Comparison of the experimental and calculated surface-integrated electron heat flux versus normalised ion gradient. Analysis done at $\rho_{tor} = 0.27$.

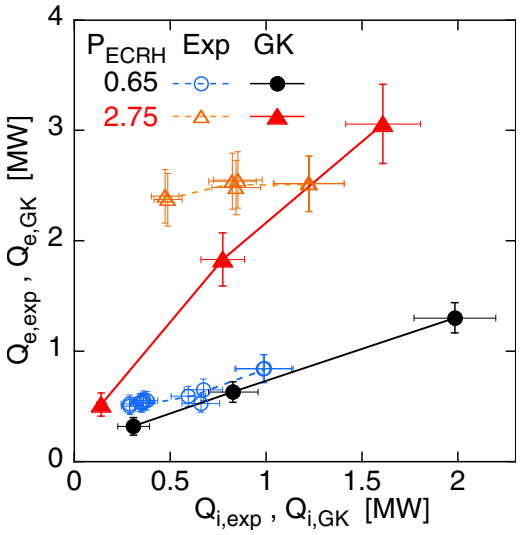

Figure 13. Experimental and calculated surface-integrated electron heat flux versus respective ion heat flux for the three NBI configurations and the two ECRH powers. Analysis at $\rho_{tor} = 0.27$.

As a complement to this plot, we show in figure 13 Q_e versus Q_i from experiment and modelling. We consider first the gyrokinetic calculations: Q_e increases roughly linearly with Q_i but with a slope which depends on the applied electron heat flux through P_{ECRH}. For the

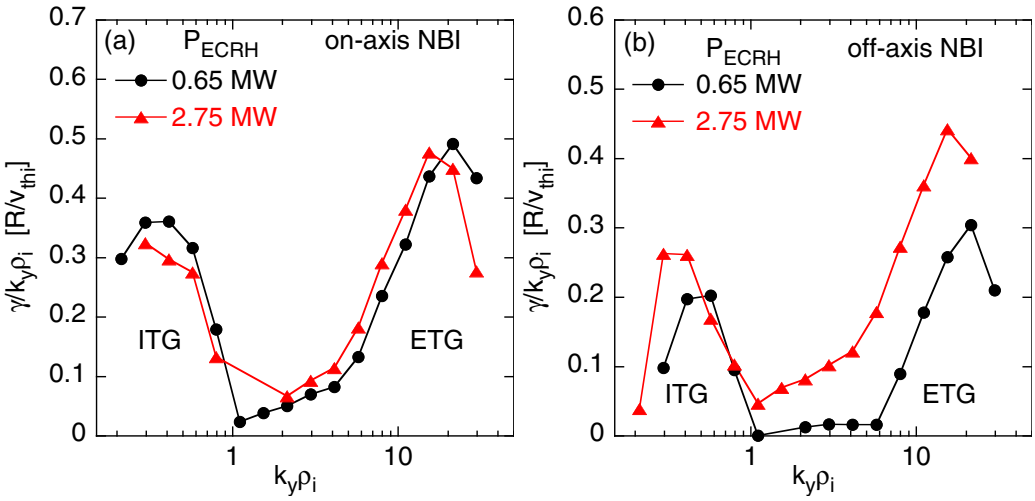

Figure 14. Spectra from linear calculations covering the ITG-ETG wave length range, with the parameters taken at $\rho_{tor} = 0.27$. Plot (a) on-axis NBI case for the two ECRH powers. Plot (b) off-axis NBI case for the two ECRH powers.

low ECRH power case the slope corresponds roughly to $Q_e \approx 0.65 Q_i$ while it is much steeper for the high ECRH case with $Q_e \approx 2Q_i$. Therefore, already indicated above, the calculated Q_e reacts to the ECRH power. The comparison with the experimental points indicates that for the on-axis NBI cases the agreement is acceptable, whereas the calculated value is somewhat too high. This plot suggests that a reduction in Q_i, as discussed in the previous section, would also reduce Q_e and yield a better agreement for Q_e for the on-axis NBI cases. The other points of this plot for the high ECRH power also indicate clearly the strong discrepancy between experiment and modelling for off-axis NBI, as well as the rather poor agreement for the mixed case. For the off-axis case at low ECRH power the agreement is also poor. Thus, as already indicated above, in such cases with rather low ion heat flux and low R/L_{T_i}, an electron instability, TEM and/or ETG, must contribute to the electron heat flux drive.

This is investigated in the two plots of figure 14 which display the results of the linear gyrokinetic calculations over the ITG/TEM to ETG wavelength range. Plotted here is the normalised growth rate of the instabilities, versus the normalised inverse wavelength, $k_y\rho_i$. The spectra of plot (a) corresponding to the two on-axis NBI cases with the different ECRH powers exhibit two peaks, one in the ITG/TEM wave length range (low $k_y\rho_i$) and one in the ETG range (high $k_y\rho_i$). These spectra exhibit only small differences between the two

ECRH power and the two peaks have about the same amplitude. This is coherent with the fact that the non-linear calculations of Q_e (made in the low $k_y\rho_i$ range) agree rather well with the experiment. In contrast, the cases with off-axis NBI displayed in plot (b) reveal strong differences between the two ECRH powers. The ITG peaks remain comparable for the two ECRH powers, but for the high ECRH power the ETG peak is much higher and broader than for the low ECRH power. This clearly indicates that in this case the ETG is strongly destabilised by the increased ECRH power to contribute to the imposed electron heat flux. This is in agreement with the results of recent multi-scale gyrokinetic simulations [36, 37] and with the improved quasi-linear multi-scale saturation rule discussed in [38]. From this it can be expected that in the case with high ECRH power and off-axis NBI the ETG turbulence is more strongly destabilised and provides a significant contribution to the imposed electron heat flux.

The development of the ETG instability to drive the imposed electron heat flux has been investigated in more details in dedicated experiments described in the next subsection.

3.2. Scan of the electron heat flux

The aim of the experiments was to search for the evidence of the appearance of an electron instability above a certain level of electron heating power in addition to the NBI power. The plasma discharges are rather similar to those performed for the study described above: same plasma current (0.8 MA) and magnetic field (2.6 T), but in this case we applied constant central NBI of 5 MW throughout the discharge.

To investigate the electron heat transport, we increased the electron heat flux with the method which consists in varying the electron heat flux by applying on-axis and off-axis electron heat deposition keeping the sum approximately constant. For this purpose, we applied ECRH power deposition rather centrally ($\rho_{tor} \approx 0.25$) and more off-axis ($\rho_{tor} \approx 0.65$) varying the ratio $P_{ECRH}(0.25)/P_{ECRH}(0.65)$. The resulting variation of the electron heat flux is illustrated in figure 15 by a selection of some cases. The lowest curve corresponds to full off-axis ECRH and therefore the heat flux in the region $\rho_{tor} < 0.6$ is only due to the NBI. The highest curve corresponds to the full on-axis ECRH case. As schematically indicated in the plot, the ECRH power deposition profile is narrow, with a width of $\rho_{tor} \approx 0.1$, the two

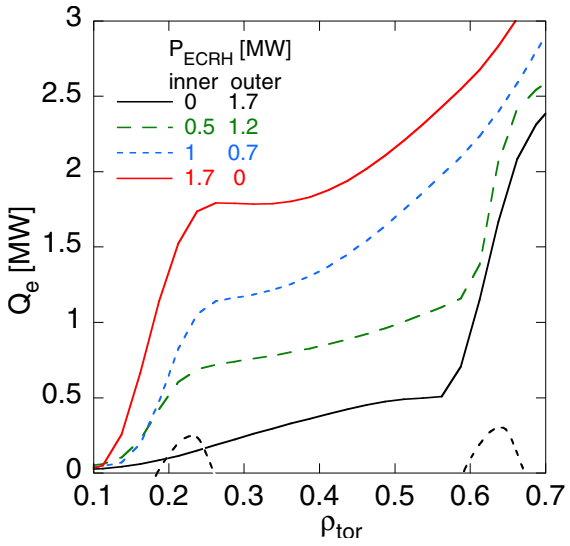

Figure 15. Profiles of the surface-integrated electron heat flux in the variation of the electron heat flux with ECRH, as described in the text. The ECRH on-axis off-axis power depositions are indicated schematically.

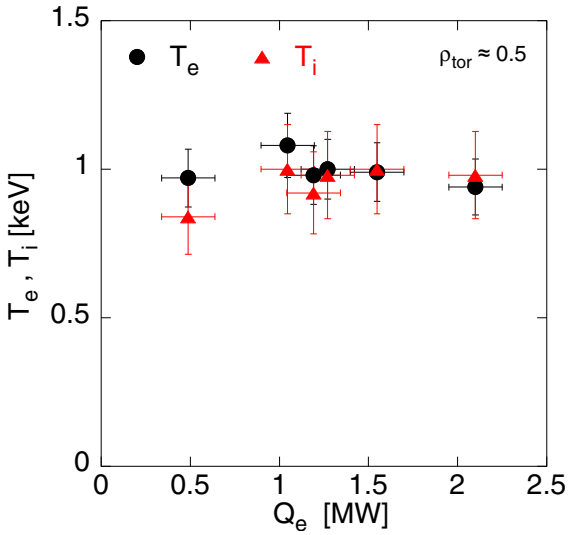

Figure 16. Experimental values of T_e and T_i at $\rho_{tor} \approx 0.5$ in the variation of the electron heat flux through ECRH, as described in the text.

depositions do not overlap and this induces a variation of the electron heat flux at $\rho_{tor} \approx 0.5$ of about 1.5 MW in addition to the constant heat flux provided by the NBI which is just below 0.5 MW.

Figure 16 shows that T_e and T_i at $\rho_{tor} = 0.5$ vary little in this scan, T_e/T_i is close to unity

which is due to the rather high density, which increases the electron-ion energy exchange ($\propto n^2$) in comparison to the previous cases and also to the fact that the analysis is made further out in radius such that the impact of energy exchange in bringing the temperatures together is stronger. As a consequence, the ITG instability is not strongly destabilised which favours the development of an electron instability when the electron heat flux is increased, as will be shown below.

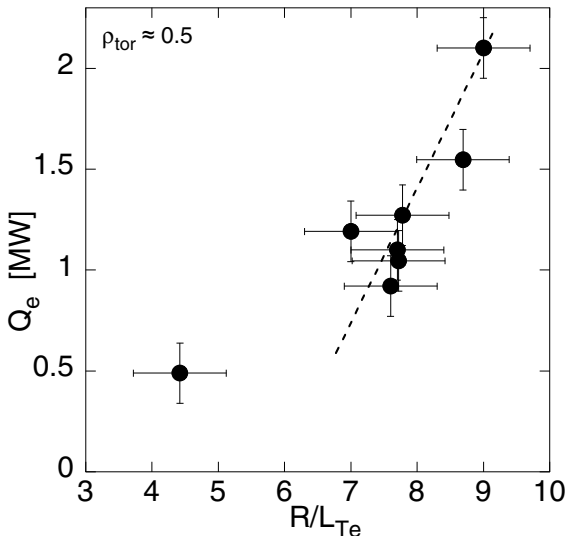

Figure 17. Experimental values of Q_e versus R/L_{T_e} at $\rho_{tor} \approx 0.5$ in the variation of the electron heat flux through ECRH, as described in the text. The point in the lower left corner is the flux due to NBI only, no central ECRH.

Figure 17 reveals a clear increase of the electron heat flux with R/L_{T_e} at $\rho_{tor} = 0.5$. The dashed line represents the linear fit to the points with ECRH, excluding the one point with NBI only. It suggests that a value of R/L_{T_e} around 6.5 at the level of Q_e for NBI alone could be interpreted as the threshold for an electron instability reflected by the strong increase of Q_e above $R/L_{T_e} \approx 6.5$ for a moderate increase in R/L_{T_e}. We will show below that this can be, here also, interpreted as the development of the ETG instability above its threshold.

As indicated above, the analysis of the electron perturbative transport provided by modulating the electron temperature with ECRH reveals the existence of an electronic instability in the transport mechanism and the related threshold if R/L_{T_e} is varied in the required range. Here we applied a 100 Hz modulation with an amplitude of about 150 kW to the deposited ECRH power, either at $\rho_{tor} = 0.25$ or $\rho_{tor} = 0.65$. The induced T_e modulation

allows us to analyse the perturbative electron transport around $\rho_{tor} = 0.5$ yielding χ_e^{HP} and compare it to χ_e^{PB}. To ensure good T_e data deduced from the modulated ECRH the ELMs were mitigated with edge magnetic perturbations which requires a density of about 7 $10^{19}\mathrm{m}^{-3}$ in the high collisionality branch, [39]. The results of this analysis are shown in figure 18 which reveals a weak increase of χ_e^{PB} with R/L_{T_e} but a strong increase of χ_e^{HP} above $R/L_{T_e} \approx 7$. This suggests that the R/L_{T_e} threshold for this active instability is close to 7. This is consistent with the threshold suggested by the heat flux analysis of figure 17. These results provide a clear evidence for the development of an electron instability above $R/L_{T_e} > 7$.

Similarly to the study described in the previous subsection, linear gyrokinetic calculations were performed over a large range of turbulence wavelengths which cover the ITG/TEM to ETG ranges. Here, the value of R/L_{T_e} has also been varied in the range of the experiment, from 4 to 12. The spectra yielded by the linear calculations for the different values of R/L_{T_e} are shown in figure 19, normalised growth rates versus $k_y\rho_i$. As in figure 14 they exhibit two peaks, one in the ITG range and the other in the ETG range. The latter exhibits a clear increase of the growth rates with R/L_{T_e} while the effect of R/L_{T_e} is much smaller in the $k_y\rho_i$ range corresponding to ITG/TEM. The analysis of the rotation of the modes indicates that the high $k_y\rho_i$ are due to electron modes, therefore ETG, while the low $k_y\rho_i$ are

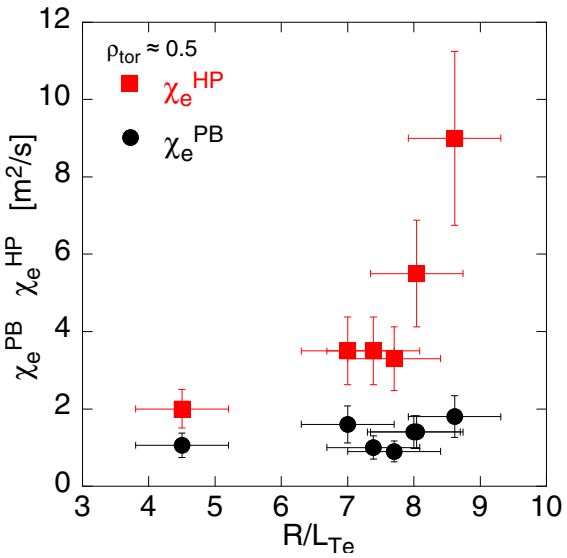

Figure 18. Experimental values of χ_e^{PB} and χ_e^{HP} versus R/L_{T_e} at $\rho_{tor} \approx 0.5$ in the variation of the electron heat flux through ECRH.

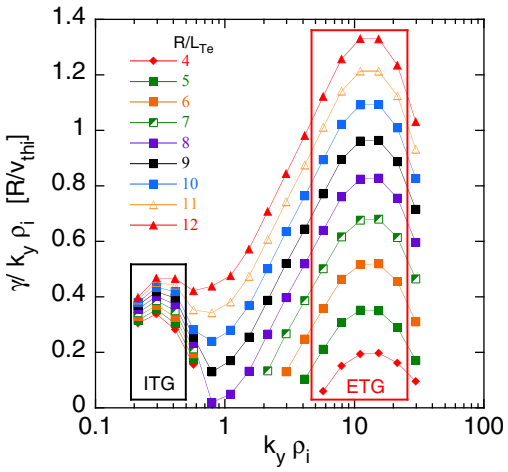

Figure 19. Spectra of the linear gyrokinetic calculations at $\rho_{tor} = 0.5$ for the electron heat flux scan and the corresponding variation in R/L_{T_e}. This shows a contour plot of the normalised growth rate versus normalised inverse turbulence wavelength for different values of R/L_{T_e}.

strongly dominated by the ITG. The turbulence rotation associated with the spectra of figure 19 indicate that for all values of R/L_{T_e} the turbulence is of ion type (ITG) for $k_y\rho_i \leq 0.5$ For $k_y\rho_i \geq 1$ the turbulence is of electron type (TEM and/or ETG) for all values of R/L_{T_e}. This behaviour of the spectra is in agreement with the expectations: a weak destabilisation of the ITG with increasing R/L_{T_e} and a strong increase of the electron turbulence with increasing R/L_{T_e}. The intermediate range $0.5 < k_y\rho_i \leq 0.8$ is a zone of transition in which the ion turbulence is present for lower R/L_{T_e} and electron turbulence for higher values of R/L_{T_e}. The electron turbulence corresponding to values of $k_y\rho_i$ in the range 0.8 - 2 can be considered as TEM, while higher values of $k_y\rho_i$ are attributed to the ETG, as schematically indicate in figure 19 by rectangles. These spectra indicate that the growth rate in the TEM range remains much weaker that in the ETG range. According to the criterion for the saturation rule in multi-scale calculations presented in [38], the fact that the peak in the ETG range exceeds that of the ITG/TEM range for R/L_{T_e} values above 6-7 indicates a significant contribution to electron heat transport by the ETG towards high R/L_{T_e}. The heat transport driven by the ETG turbulence is higher than expected solely from its small scale thanks to the appearance of streamers [26] and is named “streamer regime” in [38]. Therefore, increasing the electron heat flux under the conditions of our experiments destabilises the ETG much more than the TEM such that the relative contribution of the TEM to electron heat transport is much weaker

than that of the ETG with streamers.

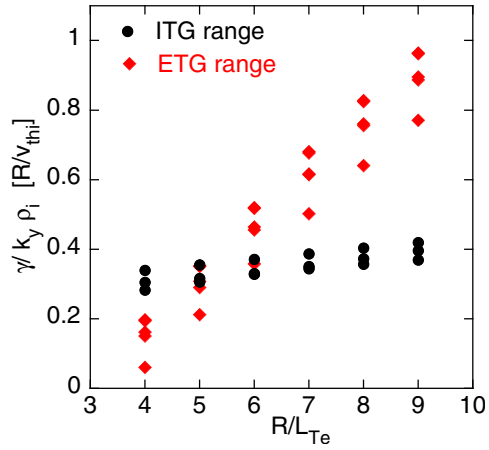

Figure 20. Results of the linear gyrokinetic calculations for the ITG and ETG selection of $k_y\rho_i$ ranges shown in figure 19 by the two rectangles. This illustrates the strong increase of the normalised growth rate for the ETG while that of the ITG is weak.

Selecting ranges representative for the ITG and ETG as indicated in figure 19 by the two rectangles and plotting in figure 20 these normalised growth rate values versus R/L_{T_e} indicates clearly the increase of the ETG activity above $R/L_{T_e} \approx 6$ while the ITG varies little. This is in quantitative agreement with the increase of χ_e^{HP} shown in figure 18, confirming the appearance of the ETG.

There is a difference between the two sets of experiments. While in the variation of the NBI configurations the ETG instability was strongly destabilised with high ECRH power in the off-axis but not in the on-axis NBI cases, here the ETG is strongly destabilised with a similar power of on-axis NBI. We attribute this difference to the different values of T_e/T_i which is close to unity in the present case while it reached two in the analysis discussed in the previous subsection. The difference in T_e/T_i has two consequences: the higher temperature ratio destabilises the ITG such that the electron heat flux is high but it stabilises the ETG, in particular through the threshold which is higher. Conversely, for the case with $T_e/T_i \approx 1$, the ITG is more stable and the ETG less stable explaining that the ETG can become active in the ECRH scan despite of the on-axis NBI.

4. Summary and discussion

We presented a study of ion and electron heat transport in H-modes whereby for each of the channels the heat flux has been varied using a variation between on-axis and off-axis power deposition. The ion heat flux was varied with NBI, the electron heat flux and the T_e/T_i ratio with ECRH. This provided two series of H-modes to study the ion heat flux at two different values of T_e/T_i while the electron heat flux could be investigated in these two series and in a dedicated scan of the electron heat flux.

The ion heat flux, which is driven by the ITG, exhibits the behaviour predicted by theory and confirmed by gyrokinetic modelling for these experiments as follows:

- The existence of a threshold in R/L_{T_i} above which the heat flux increases is seen without ambiguity. The estimates of the threshold from modelling and experiment agree well.
- The destabilisation of the ITG instability at higher T_e/T_i is evidenced. Our results show clearly that it leads to a somewhat lower threshold in R/L_{T_i} but more important to a stronger stiffness such that the T_i profiles are forced to be closer to the R/L_{T_i} threshold for a given ion heat flux which significantly affects the T_i profiles. These effects of high T_e/T_i are quantitatively well reproduced by the modelling results. Whether this is only due to the direct impact of T_e/T_i on the ITG stability or that an additional effect of the temperature ratio on the ITG stabilisation by the fast ions also contributes could not be clarified within the frame of the present work.
- The stabilisation by the NBI fast ions is strong whereby in the case of the highest stabilising effect the flux reduction in the gyrokinetic calculation seems somewhat too weak but the accuracy of the comparison depends on uncertainties on the estimate of the fast ion density profile.

As known for more than two decades, the T_e/T_i ratio plays a role on confinement. High confinement is generally obtained with low T_e/T_i values, yielding high values of T_i and R/L_{T_i} as a results of low ion heat transport corresponding to the weak ITG activity.

Conversely, applying electron heating often induces a reduction of T_i and R/L_{T_i} which is deleterious for confinement, see for instance [40, 41, 42, 43, 33]. Our results on the effect of T_e/T_i are therefore in line with previous results and in addition evidence explicitly the impact of the

change in stiffness. This also explains why comparisons based on the T_e/T_i dependence of the ITG threshold only are regularly found to under-predict the negative impact of an increase of T_e/T_i on the confinement, since, as demonstrated in the present work, the change in stiffness causes an even stronger negative effect.

The expected stabilising effect by fast ions, here from NBI, is found in our study, in agreement with recent publications [29, 30, 31, 32, 33]. Our results indicate without doubts that this stabilisation decreases the stiffness and suggest an increase of the threshold, the latter cannot be demonstrated experimental though, because decreasing the ion heat flux, from off-axis to on-axis NBI, is correlated with a reduction of the fast ion density. Note that this would also be the case for ICRH. This stabilisation is of course favourable for high T_i. In this frame, even at fixed T_e/T_i value, which is possible in the experiments if the ratio of ion to electron heating can be adjusted, the points with different ion heating and fast ion population do not belong to the same threshold-stiffness curve in the (q_i, R/L_{T_i}) diagram, with or without gyro-Bohm normalisation. Consequently, as clearly demonstrated by our study, the interpretation of experimental results on q_i versus R/L_{T_i} requires comparison with modelling including the relevant effects. Further analysis based on quasilinear modelling is being carried out [44].

Furthermore, in the on-axis off-axis experiments it is also essential to keep the boundary condition of the temperature profiles constant outside of the region where the heat flux is varied, which is the case in our study. It is indeed well-known that T_i in the core is roughly proportional to the boundary temperature (e.g. pedestal top), [45, 46, 47]. Therefore a variation of T_i at the boundary can introduce a T_i variation at the radial position of the analysis may induce a misleading interpretation, in particular through the $T_i^{2.5}$ of the gyro-Bohm normalisation.

An analysis of the properties of the ion heat flux has been carried out in the DIII-D tokamak, [48]. It should be pointed out that this tokamak is very similar to ASDEX Upgrade, both in size and physics parameters such that one expects the physics results to be similar. In these DIII-D experiments the heat flux has been varied by NBI power scans using NBI on-axis deposition with either co-injection and counter-injection, providing the possibility to investigate the effect of plasma rotation, which cannot be done in AUG. These results yield a weak impact of plasma rotation on ion heat transport which is therefore in line with our data. This study yields a power scan for two different classes of plasmas, low and high NBI

torque. These two sets of experiments based on scans of the NBI power deposited centrally probably induced, in addition to the variation of R/L_{T_i}, from changes of quantities impacting on the ITG stability and gyro-Bohm normalisation: T_i (including pedestal top), NBI fast ion content and possibly T_e/T_i. For each plasma of these two classes the ion heat transport has been analysed yielding plots of the ion heat flux in gyro-Bohm units versus R/L_{T_i}. In contrast to our results, these plots exhibit a clear *decrease* of $q_{i,gB}$ with increasing R/L_{T_i} and therefore not any indication of threshold and stiffness behaviour. It is indicated in reference [48] that the predicted variations of the ITG threshold with T_e/T_i are not sufficient to explain the measured change in experimental values of R/L_{T_i} or to hide the threshold-stiffness behaviour. It is therefore concluded in [48] that the hypothesis of "stiff transport" does not apply to these experiments or that the stiffness is very weak. The difference between the results obtained in the two devices can be due to the way the experiments have been conducted, such that the impact of the various physics quantities on the ITG stability vary. Our study indicates that the stabilisation by the fast ions can be strong enough to significantly reduce the stiffness, therefore leading indeed to a weak stiffness. This could explain the results of the DIII-D experiments in which a significant content of NBI fast ions can be expected as the density was lower than in our experiments and the NBI power higher. As further experimental difference, one may speculate that in the DIII-D experiments the pedestal ion temperature might increase with the ion heat flux of the NBI power scan. Such a change of the boundary condition for T_i would cause an increase of T_i in the core, which in turn reduces the gyro-Bohm normalised ion flux through the $T_i^{2.5}$ normalisation but does not reflect the actual physics transport properties, as already discussed above. Therefore, one might speculate that in the DIII-D experiments an increase of T_i due to the combined effects of fast ion stabilisation and pedestal temperature could yield this unexpected behaviour of $q_{i,gB}$ through the $T_i^{2.5}$ dependence of the gyro-Bohm normalisation and therefore hide the stiffness behaviour. The cause of the difference between the two devices could be clarified by a quantitative comparison of the datasets in the frame of the corresponding joint experiment in the ITPA Transport and Confinement working group.

The aim of our experiment on the electron heat flux was to search for the predicted appearance of an electron instability, TEM or ETG, when the electron heat flux is increased by applying applied electron heating above a level which cannot be driven by the ITG only. This has been

achieved along two lines of experiments which are complementary. In one of them the stability of the ITG was varied by changing the ion heat flux with NBI, keeping the electron heat flux rather constant. In the other one, the ion heat flux and the ITG activity were almost not changed while the electron heat flux was increased. In both cases the ETG instability develops above a certain R/L_{T_e} threshold and contributes to the drive of the electron heat flux. The results of the linear calculations carried out for such cases indicate that the TEM instability remains weak and most probably does not contribute significantly to the electron heat transport. This is not general and related to our experimental conditions, with rather low values of T_e/T_i and high collisionality which favour the appearance of the ETG and damp that of the TEM which would require lower collisionality and higher T_e/T_i, while increasing T_e/T_i and Z_{eff} would concomitantly increase the threshold for the ETG turbulence and damp its activity. We verified in additional linear gyrokinetic calculations that the TEM instability indeed appears while the ETG is strongly damped when collisionality is decreased, T_e/T_i, density gradient and Z_{eff} increased. A detailed dedicated study is being carried out at AUG on this topic [49]. Results suggesting the appearance of the ETG with increasing electron flux have also been found in the JET tokamak, [37]. In experiments carried out in the DIII-D, in L-mode at lower density and lower NBI power [5], an electron instability appeared at high electron heat flux but is attributed to the TEM and not the ETG. These discharges were carried in conditions favourable for the appearance of the TEM and not for the ETG, such as low collisionality, $T_e/T_i > 1$ and rather high density gradient. As mentioned above, for such conditions our calculations also predict the appearance of the TEM, such that there is no contradiction between the results found in these two devices.

Acknowledgment

The authors warmly thank A. Di Siena for very valuable discussions. This work was partly performed within the framework of the EUROfusion Consortium and has received funding from the Euratom research and training program 2014-2018 and 2019-2020 under grant agreement No 633053. The views and opinions expressed herein do not necessarily reflect those of the European Commission.

References

[1] F. Ryter et al., Nuclear Fusion **43** (2003) 1396.

[2] J. C. DeBoo et al., Nuclear Fusion **45** (2005) 494.

[3] Y. Camenen et al., Plasma Physics and Controlled Fusion **47** (2005) 1971.

[4] F. Ryter et al., Plasma Physics and Controlled Fusion **48** (2006) B453.

[5] J. DeBoo et al., Physics of Plasmas (2012) 082518.

[6] B. J. D. Tubbing et al., Nucl. Fusion **27** (1987) 1843.

[7] N. J. Lopes Cardozo et al., Plasma Phys. Controlled Fusion **32** (1990) 983.

[8] A. Jacchia et al., Phys. Fluids **B 3** (1991) 3033.

[9] F. Ryter et al., Plasma Physics and Controlled Fusion **52** (2010) 124043.

[10] F. Imbeaux et al., Plasma Physics and Controlled Fusion **43** (2001) 1503.

[11] F. Ryter et al., Physical Review Letters **95** (2005) 085001.

[12] F. Ryter et al., Nuclear Fusion **51** (2011) 113016.

[13] R. Fischer et al., Fusion Science and Technology **58** (2010) 675.

[14] S. K. Rathgeber et al., Plasma Physics and Controlled Fusion **55** (2013) 025004.

[15] S. S. Denk et al., Plasma Physics and Controlled Fusion **60** (2018) 105010.

[16] R. M. McDermott et al., Plasma Physics and Controlled Fusion **53** (2011) 124013.

[17] E. Viezzer et al., Review of Scientific Instruments **83** (2012) 103501.

[18] R. M. McDermott et al., Review of Scientific Instruments **88** (2017) 073508.

[19] A. Pankin et al., Computer Phys. Comm. **159** (2004) 157.

[20] F. Poli et al., TRANSP, [Computer Software] https://doi.org/10.11578/dc.20180627.4, 2018.

[21] F. Romanelli et al., Plasma Phys. Controlled Fusion **31** (1989) 1535.

[22] S. C. Guo et al., Physics of Fluids B: Plasma Physics **5** (1993) 520.

[23] E. Asp et al., Plasma Physics and Controlled Fusion **47** (2005) 505.

[24] J. Weiland et al., Plasma Physics and Controlled Fusion **47** (2005) 441.

[25] A. Zocco et al., Journal of Plasma Physics **84** (2018) 715840101.

[26] F. Jenko et al., Physics of Plasmas **8** (2001) 4096.

[27] R. E. Waltz et al., Phys. Plasmas **5** (1998) 1784 .

[28] G. Tardini et al., Nuclear Fusion **47** (2007) 280.

[29] J. Citrin et al., Phys. Rev. Lett. **111** (2013) 155001.

[30] J. Citrin et al., Nuclear Fusion **54** (2014) 023008.

[31] A. Di Siena et al., Nuclear Fusion **58** (2018) 054002.

[32] H. Doerk et al., Nuclear Fusion **58** (2018) 016044.

[33] N. Bonanomi et al., Nuclear Fusion **58** (2018) 056025.

[34] A. Peeters et al., Computer Phys. Comm. **180** (2009) 2650 .

[35] A. Di Siena et al., Submitted to Nuclear Fusion, arXiv:1812.03755 (2019).

[36] N. Howard et al., Nuclear Fusion **56** (2015) 014004.

[37] N. Bonanomi et al., Nuclear Fusion **58** (2018) 124003.

[38] G. Staebler et al., Nuclear Fusion **57** (2017) 066046.

[39] W. Suttrop et al., Phys. Rev. Lett. **106** (2011) 225004.

[40] A. Manini et al., Plasma Physics and Controlled Fusion **46** (2004) 1723.

[41] A. Manini et al., Nuclear Fusion **46** (2006) 1047.

[42] F. Sommer et al., Nuclear Fusion **55** (2015) 033006.

[43] C. Petty et al., Nuclear Fusion **57** (2017) 116057.

[44] G. Tardini et al., In preparation for 46th European Physical Society Conf. on Plasma Physics (2019).

[45] W. Suttrop et al., Nuclear Fusion **37** (1997) 119.

[46] G. Tardini et al., Nuclear Fusion **42** (2002) 258.

[47] A. G. Peeters et al., Nuclear Fusion **42** (2002) 1376.

[48] T. Luce et al., Nuclear Fusion **58** (2018) 026023.

[49] N. Bonanomi et al., In preparation (2019).